Check for updates

Capturing the amplitude and phase profile of the vortex beam based on coherent detection

Shengmei Zhao[1,2]*, Quanqing Qiao[1] and Le Wang[1]

[1]Institute of Signal Processing and Transmission, Nanjing University of Posts and Telecommunications (NUPT), Nanjing, China, [2]Key Lab of Broadband Wireless Communication and Sensor Network Technology, Ministry of Education, Nanjing University of Posts and Telecommunications, Nanjing, China

In this study, we propose a scheme to capture the amplitude and phase profile of the orbital angular momentum (OAM) beam based on coherent detection. In the scheme, the OAM beam to be measured is interfered with a local plain wave which is prepared at the receiver, and two charge-coupled devices (CCDs) are used to record the constructive and destructive interference patterns. By setting the phase of the plain wave to $\pi/2$ and π, one can extract the amplitude and phase profile of the OAM beam from the two interference patterns. We verify the feasibility of the scheme by simulation and experiments. The results show that both amplitude and phase profiles of single OAM and OAM superposition modes can be captured by using the proposed scheme, and the proposed scheme shows strong robustness even under the presence of atmospheric turbulence.

1 Introduction

Orbital angular momentum (OAM) of light is an attractive degree of freedom for fundamental studies in classical communications [1, 2] and quantum information processing [3–5]. Since the first demonstration of that, an $e^{i\ell\theta}$ vortex phase structure of a circularly symmetric beam was found to have $\ell\hbar$ units of OAM in 1992, where $\hbar$ is Planck's constant [6], OAM has become a useful information carrier in a variety of applications [2, 7–9]. It is shown that OAM can be used together with polarization to increase the channel capacity of communication systems [10]. The usage of OAM multi-level encoding bases can increase the tolerance of quantum key distribution (QKD) systems against eavesdropping [11]. The multiplexing of OAM modes is also demonstrated to greatly increase the bandwidth efficiency both in free-space (FSO) and fiber optical communication systems [2, 12, 13].

Therefore, it is important to detect the OAM mode at the receiver end. Until now, there have been a lot of works focusing on this task [14–16]. The simplest way to detect an OAM beam is performing a projection measurement [2], where the OAM mode with ℓ topological charge is first transferred to a flat phase beam by being illuminated on a forked
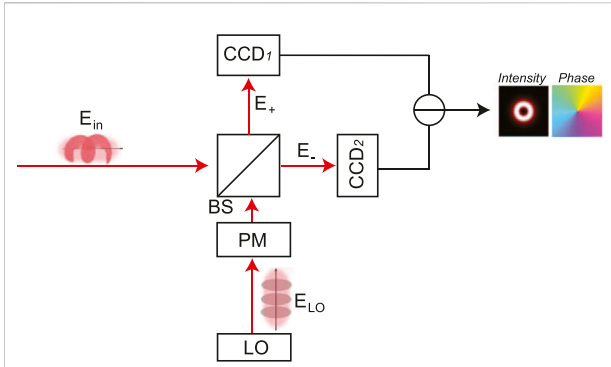
FIGURE 1
Scheme to capture the amplitude and phase profile of the OAM mode based on the coherent detection method. LO: local oscillator. PM: phase modulator. BS: beam splitter.
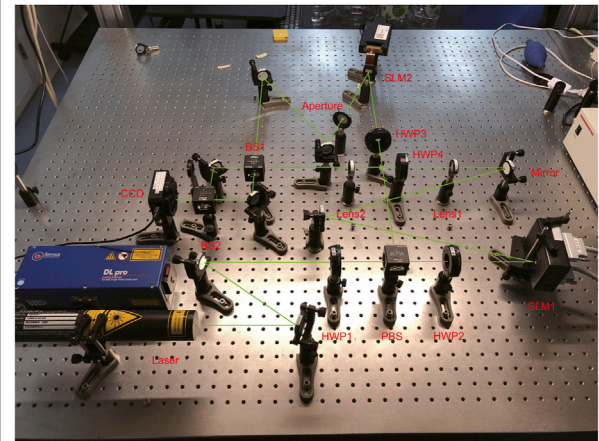

FIGURE 2
Experiment setup for the proposed scheme.

hologram with $-\ell$ and then detected by a power detector. Later, a technique for separating OAM modes by using a Mach–Zehdner interferometer at the single-photon level was presented [17]. To efficiently sort N OAM modes simultaneously, Berkhout *et al.* proposed a separating method based on the transformation from Cartesian to log-polar [18]. Also, the separation diffraction limitation was overcome by using the fan-out technique [19]. Simulations and experiments demonstrated that the separating method could distinguish the different OAM modes simultaneously with a detector array [20–22]. Thereafter, an efficient separating orbital angular momentum mode with radial varying phase was proposed [23]. Then, multiplane-light conversion, spiral transformation, and metasurfaces for combined OAM and SAM analysis were used to detect the OAM mode [24–28]. Recently, deep learning techniques were used to detect the OAM mode [29]. Also, the amplitude and phase quadratures of vortex beams are detected for testifying the quantum entanglement of vortex beams [30–34]. However, there are fewer studies carried out on capturing both the amplitude and phase profile of the OAM beam simultaneously.

In this study, we propose a scheme to capture the amplitude and phase profile of the OAM mode based on the coherent detection method. In the scheme, the receiver uses a beam splitter to integrate the OAM beam to be measured with a plain wave modulated with different phases to produce two interference patterns. Also, two charge-coupled devices (CCDs) are used to capture these patterns. By changing the phase of the plain wave with $\pi/2$ and π, one can obtain the amplitude and phase profiles of the OAM modes, including the single OAM mode and the superposition OAM mode, from the two CCD patterns.

There are some advantages of our scheme: 1) the proposed scheme could capture the amplitude and phase profile of the OAM mode simultaneously, 2) the proposed scheme can detect the single/superposition OAM modes, and 3) the scheme has strong robustness even under atmospheric turbulence.

2 Theory

Figure 1 shows the schematic diagram of the proposed scheme to capture the amplitude and phase profile of the orbital angular momentum mode based on the coherent detection method. The receiver uses a beam splitter to integrate the OAM beam to be measured E_{in} with a plain wave E_{LO} modulated with different phase φ_{PM} to produce the interference patterns. The plain wave E_{LO} is generated by a local oscillator and is then modulated by a phase modulator to obtain the phase φ_{PM}. The interference patterns E_+ and E_- are exported from the two outputs of the beam splitter. Two CCDs are used to capture the interference pattern from the two outputs of the beam splitter. By changing the phase φ_{PM} of the plain wave with $\pi/2$ and π, one can capture the amplitude and phase profile of the OAM beam E_{in} based on the interference pattern obtained from the CCDs.

The OAM mode to be measured E_{in} is assumed to be described as

$$E_{in}(r,\theta,t) = R(r)\exp(j\ell\theta)\exp(j\omega t), \qquad (1)$$

where r and θ are the radial and azimuthal coordinates, respectively; $R(r)$ and $\exp(j\ell\theta)$ denote the amplitude and spatial phase of the beam, respectively; ℓ is the OAM topological charge, which is an integer; $R(r)$ could be different mode structures, such as Laguerre–Gaussian modes or Bessel–Gaussian modes; and ω is the frequency of the OAM beam.

A plain wave E_{LO} is generated by a local oscillator (LO) at first and is defined as

$$E_{LO}(r,\theta,t) = \exp(j\omega t). \qquad (2)$$

Then, it is modulated a phase by a phase modulator (PM),

FIGURE 3
Simulation and experimental results of the proposed scheme to capture the amplitude and phase profile of single OAM beam E_{in}.

$$E_{LO}(r, \theta, t) = \exp(j(\omega t + \varphi_{PM})), \tag{3}$$

where φ_{PM} is the phase modulated by the phase modulator.

After that, a beam splitter is used to combine the received OAM beam E_{in} and the plain wave E_{LO} to produce interference patterns. The interference patterns E_+ and E_- are exported from the beam splitter, i.e.,

$$E_+(r, \theta, t) = jE_{in}(r, \theta, t) + E_{LO}(r, \theta, t), \tag{4}$$

and

$$E_-(r, \theta, t) = E_{in}(r, \theta, t) + jE_{LO}(r, \theta, t). \tag{5}$$

Two CCDs are used to detect the interference patterns. The interference pattern obtained by CCD1 should be $|E_+(r, \theta, t)|^2$, and the interference pattern obtained by CCD2 should be $|E_-(r, \theta, t)|^2$. One can obtain the difference between $|E_+(r, \theta, t)|^2$ and $|E_-(r, \theta, t)|^2$ as
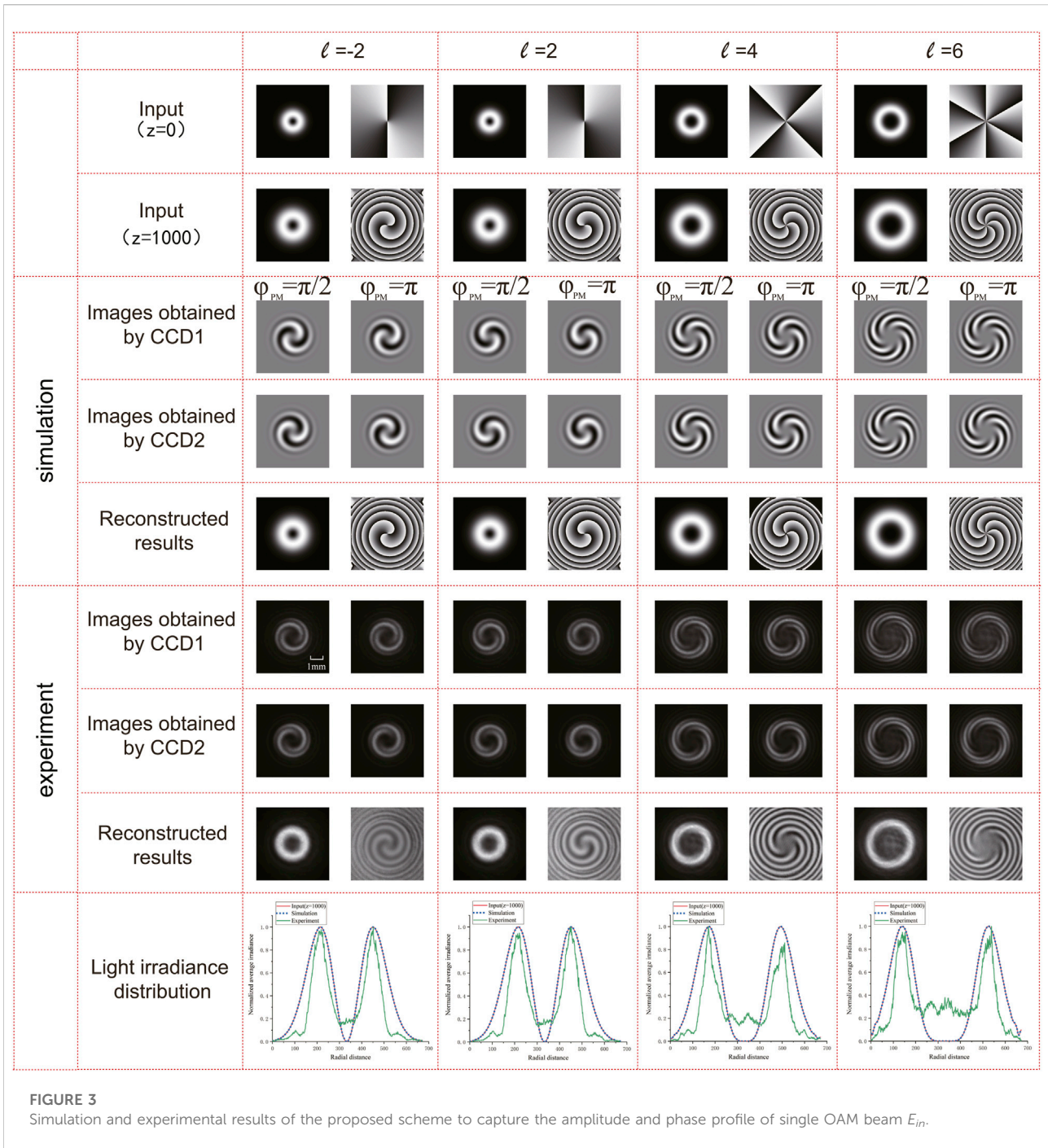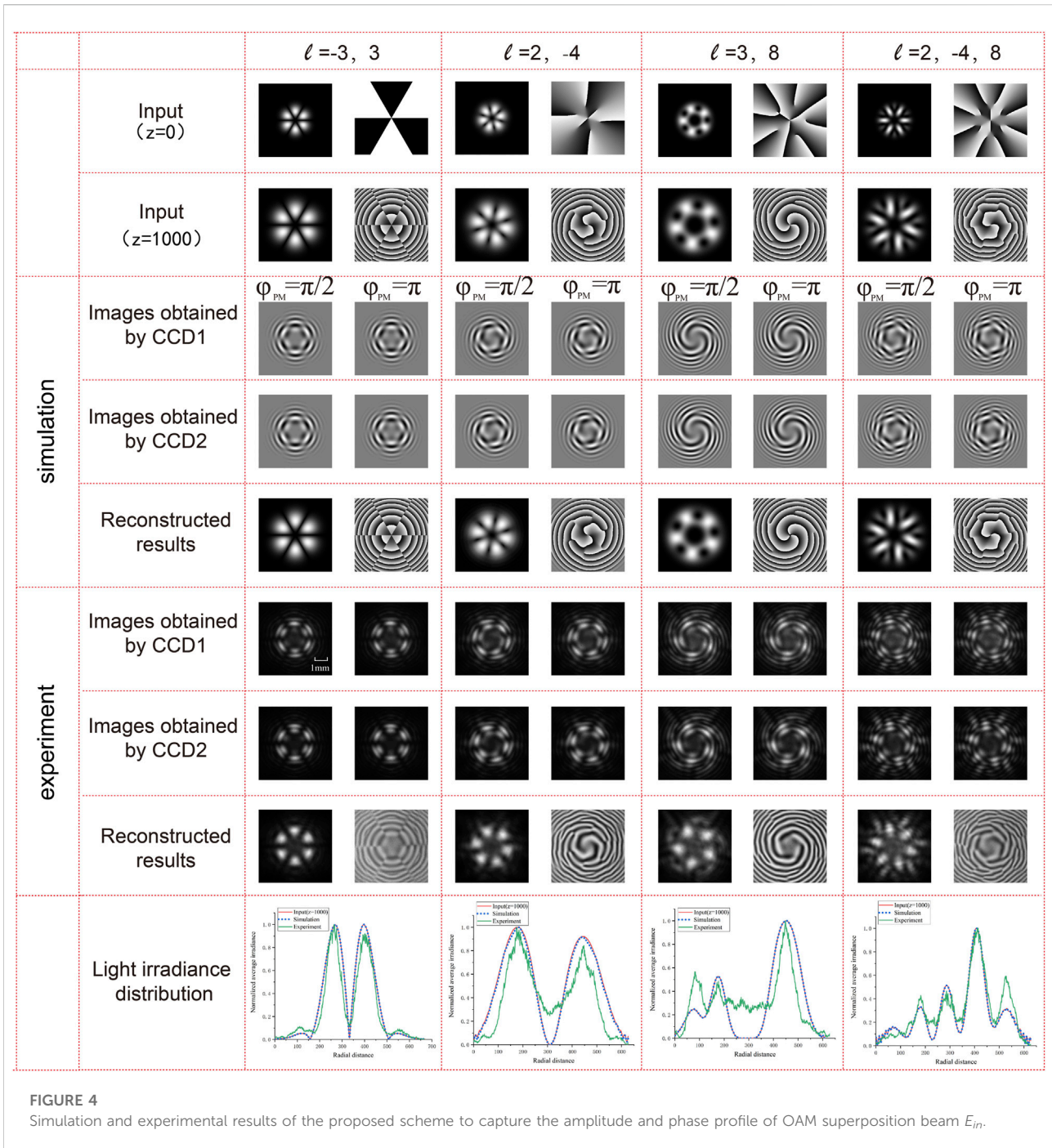
FIGURE 4
Simulation and experimental results of the proposed scheme to capture the amplitude and phase profile of OAM superposition beam E_{in}.

$$
\begin{aligned}
&|E_+(r,\theta,t)|^2 - |E_-(r,\theta,t)|^2 \\
&= |jE_{in}(r,\theta,t) + E_{LO}(r,\theta,t)|^2 - |E_{in}(r,\theta,t) + jE_{LO}(r,\theta,t)|^2 \\
&= 2jR(r)\left[\exp\left(j\ell\theta - j\varphi_{PM}\right) - \exp\left(j\varphi_{PM} - j\ell\theta\right)\right].
\end{aligned}
\tag{6}
$$

During detection, φ_{PM} is given two values for two measurements. For the first time, the modulated phase φ_{PM} is set to $\pi/2$. For the second time, the modulated phase φ_{PM} is set to π. Since Eq. 6 is related with φ_{PM}, we define the difference $|E_+(r,\theta,t)|^2 - |E_-(r,\theta,t)|^2$ as a function $f(\varphi_{PM})$, i.e.,

$$
\begin{aligned}
f\left(\varphi_{PM}\right) &= |E_+(r,\theta,t)|^2 - |E_-(r,\theta,t)|^2 \\
&= 2jR(r)\left[\exp\left(j\ell\theta - j\varphi_{PM}\right) - \exp\left(j\varphi_{PM} - j\ell\theta\right)\right].
\end{aligned}
\tag{7}
$$

By setting the phase φ_{PM} of the plain wave to $\pi/2$ and π individually, we can obtain the light field distribution of the OAM beam E_{in} based on the interference pattern obtained from the two CCDs, that is,

$$
\begin{aligned}
f(\pi/2) &= 2jR(r)\left[\exp\left(j\ell\theta - j\pi/2\right) - \exp\left(j\pi/2 - j\ell\theta\right)\right] \\
&= 4R(r)\cos\left(j\ell\theta\right),
\end{aligned}
\tag{8}
$$

FIGURE 5
Inner product results of OAM superposition beams with **(A)** ℓ = 2, − 4 and **(B)** ℓ = 2, − 4, 8.

$$f(\pi) = 2jR(r)\left[\exp\left(j\ell\theta - j\pi\right) - \exp\left(j\pi - j\ell\theta\right)\right]$$
$$= 4R(r)\sin\left(j\ell\theta\right), \qquad (9)$$

and

$$E_{in}(r, \theta) = R(r)\exp\left(j\ell\theta\right) = \frac{1}{4}\left[f\left(\pi/2\right) + jf\left(\pi\right)\right]. \qquad (10)$$

Therefore, the amplitude profile should be

$$Amplitude\{E_{in}\} = R(r) = abs\left\{\frac{1}{4}\left[f\left(\pi/2\right) + jf\left(\pi\right)\right]\right\}, \qquad (11)$$

and the phase profile should be

$$Phase\{E_{in}\} = \ell\theta = angle\left\{\frac{1}{4}\left[f\left(\pi/2\right) + jf\left(\pi\right)\right]\right\}. \qquad (12)$$

3 Results and discussion

In this section, we discuss the performance of the proposed scheme. The experimental setup for the proposed scheme is shown in Figure 2. A linear fundamental mode Gaussian beam (waist radius $\omega_0 = 0.8mm$) at a wavelength of 633 nm is generated by a He–Ne laser (Thorlabs, Model HRP020-1). After being reflected by two mirrors, the beam passes through a half-wave plate (HWP1) to adjust the intensity ratio of the two Gaussian beams after splitting. A polarization beam splitter (PBS) is used to separate and polarize the incident Gaussian beam to two beams. Then, each Gaussian beam passes through a half-wave plate (HWP1 and HWP2) to match the polarization direction of the Spatial Light Modulator (SLM1, Hamamatsu, Model X10468-07, SLM2, Holoeye, Model PLOTO-VIS-006-A). After that, each Gaussian beam is diffracted by a computer-controlled SLM. SLM1 carries a phase hologram of $\pi/2$ or π (the same function as the phase modulator), and SLM2 carries a special

phase hologram for the LG mode of different topological charges ℓ. The Gaussian beam needs to pass through another half-wave plate (HWP3) to equalize the polarization of the two beams so as to satisfy with the superposition conditions. At the same time, one aperture is used to filter out the first-order diffracted light from the diffracted beam, and two convex lenses (focal length f1 = 100 mm, f2 = 200 mm) are used to amplify the Gaussian beam. Thereafter, the two outcoming beams interfere at a beam splitter (BS1). For simultaneous measurement, two mirrors and beam splitter (BS2) are used to focus the two output beams of BS1 on a plane so that the two output beams can be captured by one CCD (Thorlabs, Model BC106N-VIS/M, 989 × 745 pixels of 8.8 mm × 6.6 mm size) at one time.

Then, we demonstrate the proposed scheme for the single OAM mode in Figure 3. The upper part is the simulation results, and the lower part is the experimental results. The topological charges ℓ for the measured OAM mode are setup to $\ell = -2$, $\ell = 2$, $\ell = 4$, and $\ell = 6$. In order to compare the performance, we also list the intensity and phase distribution of the input OAM beam (z = 0) and the input OAM beam (z = 1000 m) at the first two rows, where z is the propagation distance. It is can observed that the intensity and phase distribution are diverged with the propagation distance in comparison with for the input OAM beam (z = 0). *Images obtained by CCD1* and *Images obtained by CCD2* are the interference patterns obtained by CCD1 and CCD2, respectively, representing the constructive and destructive interference patterns, and *Reconstructed results* are the amplitude and phase profile of the OAM beam recovered by the proposed scheme. The simulation and experimental results show that our scheme has the ability to capture the amplitude and phase profile of the input OAM beam E_{in} accurately. For example, the interference patterns formed by the input OAM beam with $\ell = 2$ is a "pinwheel-shaped" pattern with two stripes

FIGURE 6
Simulation and experimental results of the proposed scheme to capture the amplitude and phase profile of the OAM beam ($\ell = 5$) under the presence of atmospheric turbulence.
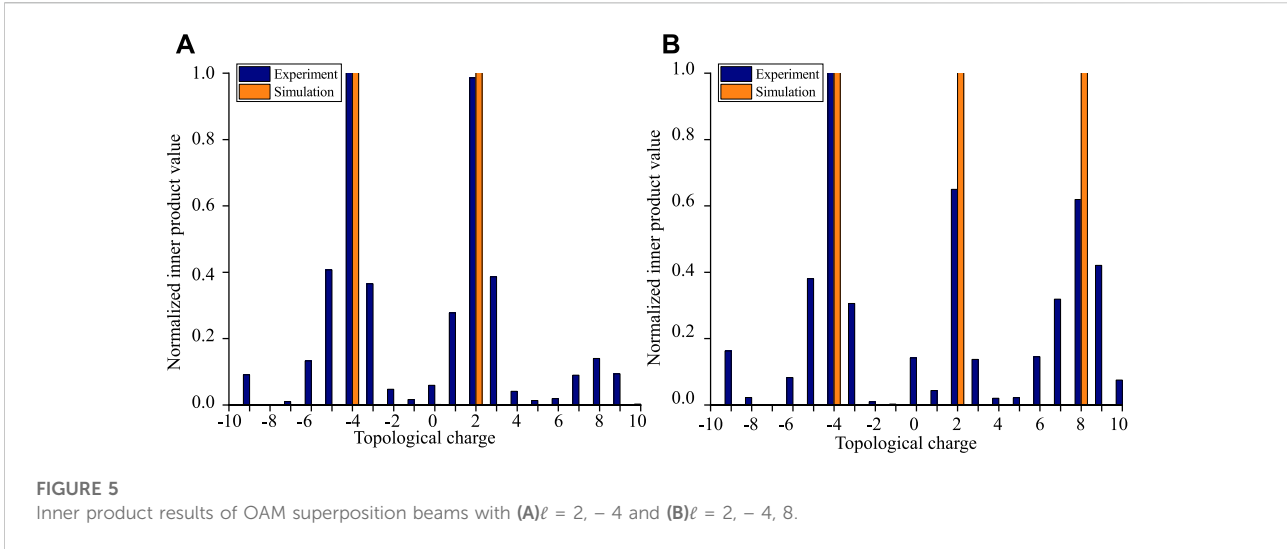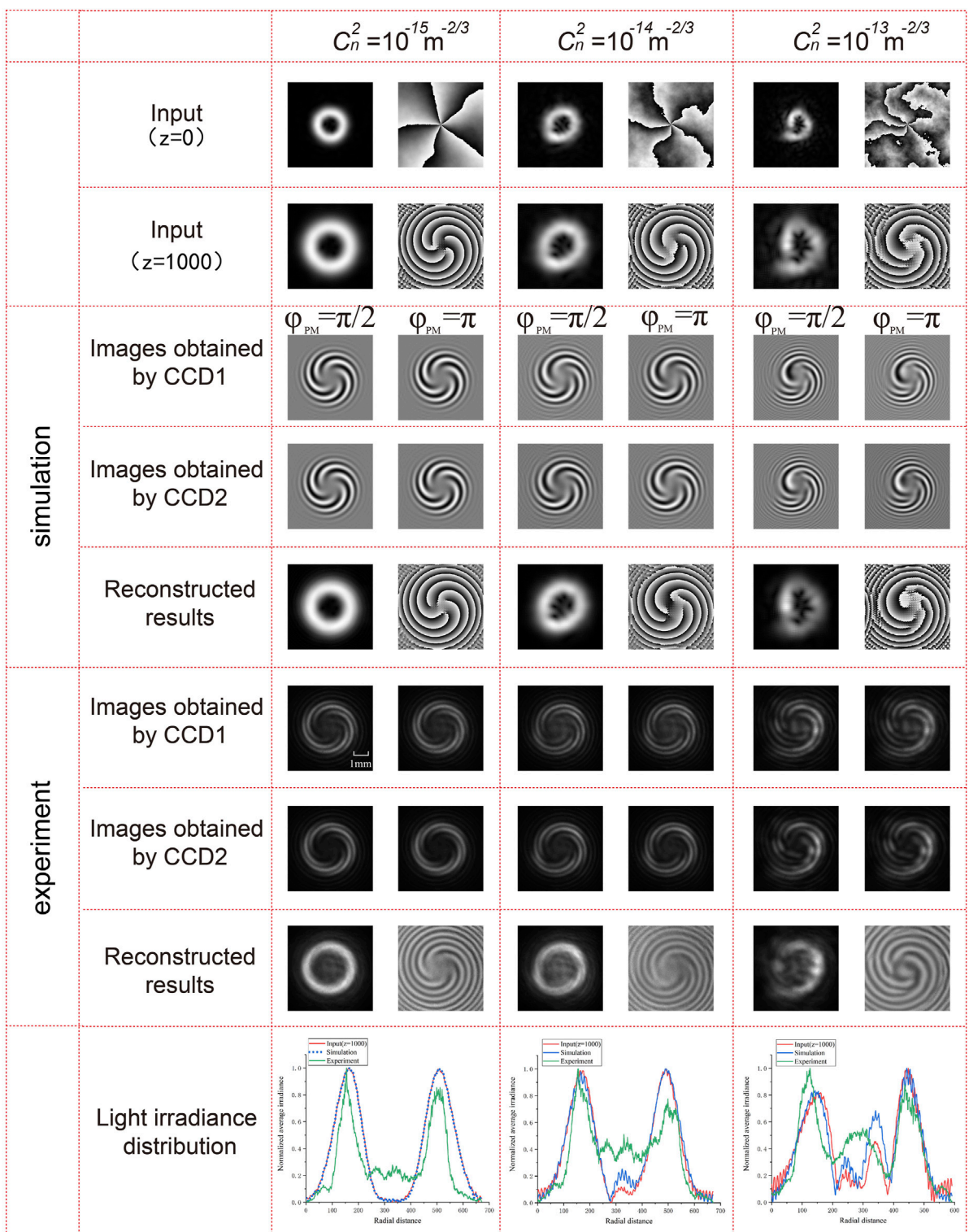
TABLE 1 Peak signal-to-noise ratio of simulation and experimental results.

PSNR	ℓ								C_n^2		
	-2	2	4	6	$-3, 3$	$2, -4$	$3, 8$	$2, -4, 8$	10^{-15}	10^{-14}	10^{-13}
Amplitude	19.4	19.07	16.26	14.71	17.78	18.97	18.29	18.37	15.72	16.69	17.08
Phase	13.04	12.5	8.95	9.37	11.07	12.97	9.44	10.76	9.96	10.88	9.5

and clockwise rotation both in simulation and experiment, while they are "pinwheel-shaped" pattern with two stripes and counterclockwise rotation for the input OAM beam with $\ell = -2$. Comparing with the simulation results, the experimental results show the same characteristic distribution of the interference patterns and phase patterns, including the rotation direction and number of "pinwheel-shaped" stripes, but with some blurring in the patterns, which is caused by the noise in experiment. *Light irradiance distribution* further demonstrates the consistency among the input OAM beams, the simulation results, and the experimental results. Here, the input OAM beams are those OAM beams with propagation distance (z = 1000 m). Since there always exists the propagation of the beams in experiment, we use the input OAM beams with propagation distance for comparison.

Then, we further verify the case when the incident beam is an OAM superposition beam in Figure 4. Here, the selected OAM superposition beams are composed by two or three OAM modes, such as $\ell = -3, 3$, $\ell = 2, -4$, $\ell = 3, 8$, and $\ell = 2, -4, 8$. Also, the intensity and phase profile of the superposition OAM beams are demonstrated in the first and the second row, followed by the interference patterns obtained at CCD1 and CCD2, and the last row is the recovered results by using the proposed scheme. Different from the single OAM mode, the intensity profile of the superposition OAM modes becomes bright and dark petal patterns, and the singular points in the phase profile are more complex, especially for the superposition mode composed by more OAM modes. The upper part is the simulation results, and the lower part is the experimental results. The simulation and experimental results show that both interference patterns and captured amplitude and phase patterns have the same distribution, including the number and shape of petals. It is indicated that our proposed scheme also has the ability to capture the amplitude and phase profile of the OAM superposition beam E_{in} accurately. *Light irradiance distribution* also demonstrates the similarity among the input OAM beams, the simulation results, and the experimental results.

Based on the mutual orthogonality of OAM beams with different topological charges, we can obtain the topological charge composition of OAM superposition beams according to the reconstructed amplitude and phase profile. Firstly, the amplitude and phase profile are combined into an OAM

beam, and then the topological charge composition of OAM superposition beams can be obtained by inner product with OAM beams with different topological charges ($\ell = 10, -9, ..., 9, 10$). Figure 5 shows the inner product results of OAM superposition beams with $\ell = 2, -4$ and $\ell = 2, -4, 8$. It can be seen from the figure that we can detect the topological charge of OAM superposition beams based on the reconstructed amplitude and phase profile. There are some differences between the simulation and experiment detection results. The reason is that it is hard to locate the center of the experimental "reconstructed result", and an insignificant misalignment will cause mode crosstalk. However, one can still judge the topological charge composition according to the experimental intensity distribution.

Next, we discuss the robustness of the proposed scheme when the OAM beam is propagated under atmospheric turbulence (AT) in Figure 6. Here, we use random phase screen model simulating atmospheric turbulence [35, 36]. The simulated parameters for the random phase screen are set as follows. The wavelength λ is $633nm$, the space Δz between the two random phase screen is $200m$, the beam waist ω_0 is $0.1m$, the outer scale is $L_0 = 50m$, and the inner scale is $l_0 = 0.001m$. The topological charge of the input OAM beam is $\ell = 5$. The atmospheric refractive index structure constant C_n^2 (usually used to describe the intensity of atmospheric turbulence) is set to 10^{-15}, 10^{-14}, and $10^{-13}m^{-2/3}$. Here, one random phase screen is used for simplicity. In the experiment, the random phase screen representing atmospheric turbulence is superimposed on the OAM generating phase mask so that the input OAM mode contaminated by atmospheric turbulence is obtained when the Gaussian beam is illuminated on the SLM2 loaded by the superimposed phase distribution. It can be seen from Figure 6 that the amplitude and phase of the measured OAM beam are distorted by AT, and the stronger AT is, the larger distortion the measured OAM beam has. However, our scheme has the ability to capture the amplitude and phase profile of the OAM beam E_{in} even in this case. The simulation and experimental results show that our proposed scheme has strong robustness even under the presence of atmospheric turbulence.

The peak signal-to-noise ratio (PSNR) is often used to quantitatively estimate the recovered image quality [37], which is defined as

$$PSNR = 10\lg\left(\frac{MAX_I^2}{MSE}\right), \qquad (13)$$

where MAX_I is the maximum possible pixel value of the image. MSE is the mean square error of the image, which is defined as

$$MSE = \frac{1}{M \times N} \sum_{i=0}^{M-1} \sum_{j=0}^{N-1} \left\| f\left(x_i, y_j\right) - g\left(x_i, y_j\right) \right\|^2, \qquad (14)$$

where $g(x_i, y_j)$ and $f(x_i, y_j)$ are gray-values in (x_i, y_j) for the original and reconstructed images, respectively. $M \times N$ is the pixel of the image. Generally, the higher PSNR is, the better quality of reconstructed image is.

Finally, we calculated the peak signal-to-noise ratio (PSNR) of amplitude and phase profile captured by simulation and experiment results mentioned above to illustrate the similarity between simulation and experiment results. Table 1 shows the peak signal-to-noise ratio of the simulation and experiment results. "Amplitude" denotes the PSNR for recovered amplitude part, and "phase" denotes the PSNR for the recovered phase part. C_n^2 represents the strength of the atmosphere turbulence. The results show that the simulation and experimental results have a high degree of similarity.

4 Conclusion

In this study, we have proposed a scheme to capture the amplitude and phase profile of the incident OAM beam based on the coherent detection. With the interference between the measured OAM beam and a local plain wave, the amplitude and phase profile of the measured OAM beam could be captured by the calculation on the detection results in CCDs. The simulation and experimental results have showed that both amplitude and phase profiles can be detected by using the proposed scheme not only for the single OAM mode but also for the OAM superposition mode. Furthermore, the amplitude and phase profiles of the measured OAM beam can even be detected under the presence of atmospheric turbulence. Our method can capture the amplitude and phase profile of the input OAM beam, regardless of whether the input beam passes through atmospheric turbulence or not. At the same time, compared with the previous method which can only obtain the amplitude profile, our method can obtain amplitude and phase profile simultaneously, that is, our method can obtain

more information about the beam, so it will be more conducive for detecting topological charges in strong atmospheric turbulence environment.

Data availability statement

The original contributions presented in the study are included in the article/Supplementary Material; further inquiries can be directed to the corresponding author.

Author contributions

SZ, QQ, and LW contributed to conception and design of the study. LW performed the simulation analysis and QQ performed the experimental verification. SZ and QQ wrote the first draft of the manuscript. SZ and LW presented the revision of the manuscript. All authors contributed to manuscript revision, read, and approved the submitted version.

Funding

Conflict of interest

The authors declare that the research was conducted in the absence of any commercial or financial relationships that could be construed as a potential conflict of interest.

Publisher's note

All claims expressed in this article are solely those of the authors and do not necessarily represent those of their affiliated organizations, or those of the publisher, the editors, and the reviewers. Any product that may be evaluated in this article, or claim that may be made by its manufacturer, is not guaranteed or endorsed by the publisher.

References

1. Willner AE, Huang H, Yan Y, Ren Y, Ahmed N, Xie G, et al. Optical communications using orbital angular momentum beams. *Adv Opt Photon* (2015) 7:66–106. doi:10.1364/AOP.7.000066

2. Wang J, Yang JY, Fazal IM, Ahmed N, Yan Y, Huang H, et al. Terabit free-space data transmission employing orbital angular momentum multiplexing. *Nat Photon* (2012) 6:488–96. doi:10.1038/nphoton.2012.138

3. Malik M, Erhard M, Huber M, Krenn M, Fickler R, Zeilinger A. Multi-photon entanglement in high dimensions. *Nat Photon* (2016) 10:248–52. doi:10.1038/nphoton.2016.12

4. Wang XL, Cai XD, Su ZE, Chen MC, Wu D, Li L, et al. Quantum teleportation of multiple degrees of freedom of a single photon. *Nature* (2015) 518:516–9. doi:10.1038/nature14246

5. Zhang W, Ding DS, Dong MX, Shi S, Wang K, Liu SL, et al. Experimental realization of entanglement in multiple degrees of freedom between two quantum memories. *Nat Commun* (2016) 7:13514. doi:10.1038/ncomms13514

6. Allen L, Beijersbergen MW, Spreeuw RJC, Woerdman JP. Orbital angular momentum of light and the transformation of Laguerre-Gaussian laser modes. *Phys Rev A* (1992) 45:8185–9. doi:10.1103/PhysRevA.45.8185

7. Mair A, Vaziri A, Weihs G, Zeilinger A. Entanglement of the orbital angular momentum states of photons. *Nature* (2001) 412:313–6. doi:10.1038/35085529

8. Molina-Terriza G, Torres JP, Torner L. Twisted photons. *Nat Phys* (2007) 3:305–10. doi:10.1038/nphys607

9. Barreiro JT, Wei TC, Kwiat PG. Beating the channel capacity limit for linear photonic superdense coding. *Nat Phys* (2008) 4:282–6. doi:10.1038/nphys919

10. Malik M, O'Sullivan M, Rodenburg B, Mirhosseini M, Leach J, Lavery MPJ, et al. Influence of atmospheric turbulence on optical communications using orbital angular momentum for encoding. *Opt Express* (2012) 20:13195–200. doi:10.1364/OE.20.013195

11. Bourennane M, Karlsson A, Björk G. Quantum key distribution using multilevel encoding. *Phys Rev A* (2001) 64:012306. doi:10.1103/PhysRevA.64.012306

12. Bozinovic N, Yue Y, Ren Y, Tur M, Kristensen P, Huang H, et al. Terabit-scale orbital angular momentum mode division multiplexing in fibers. *Science* (2013) 340:1545–8. doi:10.1126/science.1237861

13. Boffi P, Martelli P, Gatto A, Martinelli M. Mode-division multiplexing in fibre-optic communications based on orbital angular momentum. *J Opt* (2013) 15:075403. doi:10.1088/2040-8978/15/7/075403

14. Leach J, Padgett MJ, Barnett SM, Franke-Arnold S, Courtial J. Measuring the orbital angular momentum of a single photon. *Phys Rev Lett* (2002) 88:257901. doi:10.1103/PhysRevLett.88.257901

15. Gibson G, Courtial J, Padgett MJ, Vasnetsov M, Pas'ko V, Barnett SM, et al. Free-space information transfer using light beams carrying orbital angular momentum. *Opt Express* (2004) 12:5448–56. doi:10.1364/OPEX.12.005448

16. Krenn M, Fickler R, Fink M, Handsteiner J, Malik M, Scheidl T, et al. Communication with spatially modulated light through turbulent air across Vienna. *New J Phys* (2014) 16:113028. doi:10.1088/1367-2630/16/11/113028

17. Leach J, Courtial J, Skeldon K, Barnett SM, Franke-Arnold S, Padgett MJ. Interferometric methods to measure orbital and spin, or the total angular momentum of a single photon. *Phys Rev Lett* (2004) 92:013601. doi:10.1103/PhysRevLett.92.013601

18. Berkhout GCG, Lavery MPJ, Courtial J, Beijersbergen MW, Padgett MJ. Efficient sorting of orbital angular momentum states of light. *Phys Rev Lett* (2010) 105:153601. doi:10.1103/PhysRevLett.105.153601

19. Mirhosseini M, Malik M, Shi Z, Boyd RW. Efficient separation of the orbital angular momentum eigenstates of light. *Nat Commun* (2013) 4:2781. doi:10.1038/ncomms3781

20. Li C, Jiang R, Wang L, Zhao SM. Simulations of high efficient separation of orbital-angular-momentum of light. *J Nanjing Univ Post Telecommun* (2016) 36:47–52. doi:10.14132/j.cnki.1673-5439.2016.03.007

21. Huang H, Milione G, Lavery MPJ, Xie G, Ren Y, Cao Y, et al. Mode division multiplexing using an orbital angular momentum mode sorter and MIMO-DSP over a graded-index few-mode optical fibre. *Sci Rep* (2015) 5:14931. doi:10.1038/srep14931

22. Huang H, Ren Y, Xie G, Yan Y, Yue Y, Ahmed N, et al. Tunable orbital angular momentum mode filter based on optical geometric transformation. *Opt Lett* (2014) 39:1689–92. doi:10.1364/OL.39.001689

23. Li C, Zhao SM. Efficient separating orbital angular momentum mode with radial varying phase. *Photon Res* (2017) 5:267–70. doi:10.1364/PRJ.5.000267

24. Fontaine NK, Ryf R, Chen H, Neilson DT, Kim K, Carpenter J. Laguerre-Gaussian mode sorter. *Nat Commun* (2019) 10:1865. doi:10.1038/s41467-019-09840-4

25. Wen YH, Chremmos I, Chen YJ, Zhu JB, Zhang YF, Yu SY. Spiral transformation for high-resolution and efficient sorting of optical vortex modes. *Phys Rev Lett* (2018) 120:193904. doi:10.1103/PhysRevLett.120.193904

26. Lei T, Fang JC, Xie ZW, Yuan XC. High-resolution cylindrical vector beams sorting based on spin-dependent fan-out optical geometric transformation. *Opt Express* (2019) 27:20901–9. doi:10.1364/OE.27.020901

27. Ruffato G, Capaldo P, Massari M, Mafakheri E, Romanato F. Total angular momentum sorting in the telecom infrared with silicon Pancharatnam-Berry transformation optics. *Opt Express* (2019) 27:15750–64. doi:10.1364/OE.27.015750

28. Wang BM, Wen YH, Zhu JB, Chen YJ, Yu SY. Sorting full angular momentum states with Pancharatnam-Berry metasurfaces based on spiral transformation. *Opt Express* (2020) 28:16342–51. doi:10.1364/OE.393859

29. Cox MA, Celik T, Genga Y, Drozdov AV. Interferometric orbital angular momentum mode detection in turbulence with deep learning. *Appl Opt* (2022) 61:D1–D6. doi:10.1364/AO.444954

30. Pan XZ, Yu S, Zhou YF, Zhang K, Zhang K, Lv SC, et al. Orbital-angular-momentum multiplexed continuous-variable entanglement from four-wave mixing in hot atomic vapor. *Phys Rev Lett* (2019) 123:070506. doi:10.1103/PhysRevLett.123.070506

31. Li SJ, Pan XZ, Ren Y, Liu HZ, Yu S, Jing JT. Deterministic generation of orbital-angular-momentum multiplexed tripartite entanglement. *Phys Rev Lett* (2020) 124:083605. doi:10.1103/PhysRevLett.124.083605

32. Wang W, Zhang K, Jing JT. Large-scale quantum network over 66 orbital angular momentum optical modes. *Phys Rev Lett* (2020) 125:140501. doi:10.1103/PhysRevLett.125.140501

33. Liu SS, Lou YB, Jing JT. Orbital angular momentum multiplexed deterministic all-optical quantum teleportation. *Nat Commun* (2020) 11:3875. doi:10.1038/s41467-020-17616-4

34. Chen YX, Liu SS, Lou YB, Jing JT. Orbital angular momentum multiplexed quantum dense coding. *Phys Rev Lett* (2021) 127:093601. doi:10.1103/PhysRevLett.127.093601

35. Zhao SM, Wang L, Zou L, Gong LY, Cheng WW, Zheng BY, et al. Both channel coding and wavefront correction on the turbulence mitigation of optical communications using orbital angular momentum multiplexing. *Opt Commun* (2016) 376:92–8. doi:10.1016/j.optcom.2016.04.075

36. Zhao SM, Leach J, Gong LY, Ding J, Zheng BY. Aberration corrections for free-space optical communications in atmosphere turbulence using orbital angular momentum states. *Opt Express* (2012) 20:452–61. doi:10.1364/OE.20.000452

37. Horé A, Ziou D. Image quality metrics: PSNR vs. SSIM. In: 2010 20th International Conference on Pattern Recognition. Istanbul, Turkey: IEEE (2010). p. 2366–9. doi:10.1109/ICPR.2010.579